Journal of Nanotechnology & Advanced Materials
An International Journal

http://dx.doi.org/10.18576/jnam/130103

Effect of Wall Permeability in Second Law Analysis of Buoyancy Driven UnsteadyChannel Flow of Nanofluids with Convective Cooling

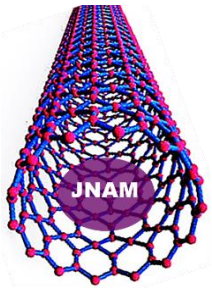

M. H. Mkwizu[1,*], *A. X. Matofali*[1], *N. Ainea*[1] *and G. K. Karugila*[1]

[1] Department of Mathematics and Statistics, College of Natural and Applied Sciences, Sokoine University of Agriculture, Morogoro-Tanzania.

Received: 3 Aug. 2024, Revised: 1 Oct. 2024, Accepted: 30 Nov. 2024
Publishedonline:1 Jan. 2025.

Abstract: This paper investigates the combined effects of wall permeability in the second law analysis of buoyancy-driven unsteady channel flow of water-based nanofluids confined between two vertical channels with convective cooling. Specifically, the study aims to: formulate a mathematical model of nanofluid flow for the case of a vertical channel with wall permeability; determine the effects of various parameters on velocity and temperature; and analyze the influence of different parameters and wall permeability on the second law of thermodynamics. Using a semi-discretization finite difference method combined with a Runge-Kutta-Fehlberg integration scheme implemented in MATLAB, the nonlinear governing partial differential equations were transformed into a system of initial value ordinary differential equations and solved numerically. The numerical results showing the effects of variations in thermophysical parameters on velocity and temperature profiles were presented graphically and discussed.

Keywords: Wall Permeability, Buoyancy, Unsteady, Nanofluids**,** Convective Cooling.

1 Introduction

Currently, fluids and heat transfer are major fields of interest due to their wide range of applications in transportation, electronics, and industrial processes. Conventional heat transfer fluids such as mineral oil, water, and ethylene glycol play a vital role in industrial applications; however, they suffer from low thermal conductivity. Choi [1] found that the addition of nanoparticles to base fluids can alter their transport properties, flow behavior, and heat transfer capabilities. This enhancement helps overcome the limitation of low thermal conductivity, which is a primary obstacle to efficient heat transfer performance. Due to their improved thermal properties, nanofluids are primarily used as coolants in heat transfer equipment such as heat exchangers, electronic cooling systems, microelectronics, and radiators.

Nanofluids are a new class of nanotechnology-based heat transfer fluids, created by dispersing and stably suspending nanoparticles with typical dimensions on the order of 10 nanometers. The term nanofluid was coined by Choi [1] to experimentally describe the enhancement of thermal conductivity in fluids containing nanoparticles. Nanofluids involve the interaction of nano-sized particles within base fluids such as water, oil, or ethylene glycol. Nanoparticles used in the preparation of nanofluids include metallic oxides (e.g., Al_2O_3, CuO), nitride ceramics (e.g., AlN, SiN), carbide ceramics (e.g., SiC, TiC), metals (e.g., Cu, Ag), semiconductors (e.g., TiO, SiO), alloyed particles (e.g., $Al_{70}Cu_{30}$), and carbon nanotubes (single-walled, double-walled, or multi-walled: SWCNT, DWCNT, MWCNT). These nanofluids have been shown to exhibit enhanced thermal conductivity, Eastman et al., [2]

There are two primary methods for the preparation of nanofluids: the single-step method and the two-step method. The single-step method involves the simultaneous production and dispersion of nanoparticles into the base fluid, typically through particle-source evaporation and direct deposition of the evaporant into the fluid. In contrast, the two-step method involves first producing nanoparticles as dry powders using chemical or physical techniques, and then dispersing the nano-sized powders into the base fluid.

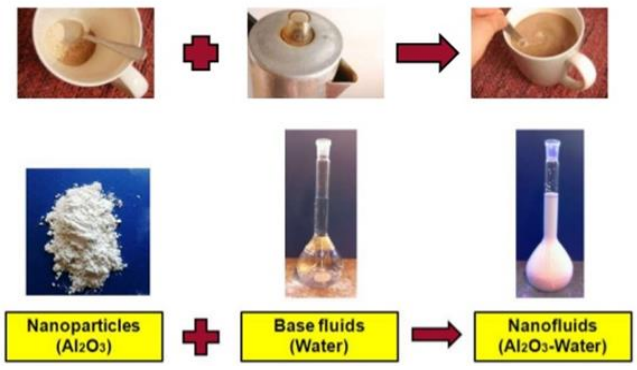

Fig. 1: Nanofuids. Source: slideshare.net

Mkwizu, Makinde, and Nkansah-Gyekye [3] conducted a numerical investigation on the second law analysis of

*Corresponding author e-mail: mkwizu@sua.ac.tz

buoyancy-driven unsteady channel flow of nanofluids with convective cooling. Their results revealed that Al_2O_3–water nanofluid achieves a higher temperature rise compared to Cu–water nanofluid. Additionally, Cu–water nanofluid exhibits higher skin friction than Al_2O_3–water nanofluid, while Al_2O_3–water nanofluid generates greater entropy than Cu–water nanofluid.

Gangadhar et al. [4] studied the electromagnetohydrodynamic (EMHD) flow of a radiative second-grade nanofluid over a Riga plate under convective heating using a revised Buongiorno's nanofluid model. Their results showed that increasing the radiation parameter and Biot number improves nanoparticle temperature distribution, while higher thermophoretic parameter values enhance nanoparticle concentration. In a complementary study, Seyyedi et al. [5] examined magneto-natural convection in a nanofluid-filled wavy-hexagonal porous enclosure, focusing on entropy generation and heat transfer. They found that raising the nanoparticle volume fraction (ϕ) increases the average Nusselt number but reduces entropy generation, with peak entropy occurring at a Hartmann number (Ha) of 14 across all aspect ratios. Specifically, when Ha = 0, increasing ϕ from 0% to 4% boosted the Nusselt number by 2.9% while decreasing entropy generation by 1.3%.

Ali and Makinde (2015) conducted a study on modeling the effect of variable viscosity on unsteady Couette flow of nanofluids with convective cooling. The results showed that, while other parameters were held constant, the velocity profile increased with an increase in the variable viscosity parameter β (or A). Temperature also increased with increasing β. The Brownian motion parameter Nb was found to reduce the rate of decrease in nanoparticle volume fraction distribution, while the thermophoresis parameter Nt exhibited the opposite effect. Skin friction increased with increasing viscosity. Additionally, the Nusselt number and consequently the convective cooling—was found to increase with an increase in the Biot number Bi.

Mkwizu et al. [7] numerically investigated the combined effects of Navier slip and wall permeability on entropy generation in unsteady generalized Couette flow of nanofluids with convective cooling. Their results demonstrated that increasing both the nanoparticle volume fraction and Reynolds number leads to a reduction in the velocity profile. The study further revealed that skin friction coefficient increases with higher nanoparticle volume fraction, larger slip parameter, and elevated Reynolds number. Notably, the entropy generation rate was found to intensify with increasing nanoparticle volume fraction and slip parameter. These findings provide valuable insights into the complex interplay between nanofluid properties, slip conditions, and thermodynamic irreversibility in permeable channel flows.

Khamis et al.,[8] conducted a study on modeling the effects of variable viscosity in the unsteady flow of nanofluids in a pipe with a permeable wall and convective cooling. They found that the nanofluid velocity and temperature reach steady-state more quickly with injection. The nanofluid flows faster with increasing values of the variable viscosity parameter, Eckert number, pressure gradient, and suction, while it slows down with increasing Biot number and injection. Additionally, the nanofluid temperature near the pipe wall increases with higher Eckert number and variable viscosity parameter but decreases due to convective heat loss to the ambient environment, following Newton's law of cooling.

Bhatti et al., [9] investigated the entropy analysis of electro-kinetically modulated peristaltic propulsion in a magnetized nanofluid flow through a microchannel. Their major findings revealed that the fluid velocity exhibited similar behavior under increasing thermal Grashof number and magnetic field strength. Furthermore, the temperature profile demonstrated a significant increase due to the combined effects of the Brinkman number and magnetic field. Additionally, the entropy profile showed a positive response, which was attributed to the dominant influence of the Brinkman number, magnetic field, and Joule heating parameter.

Abbas et al. [10] conducted an experimental investigation on entropy generation in nanofluid flow over a horizontal plate. Their study revealed that the Brownian motion parameter and thermophoresis parameter significantly enhance the temperature profile and its associated boundary layer thickness. Interestingly, the thermophoresis and Brownian motion parameters exhibited contrasting effects on the nanoparticle concentration profile. The entropy profile was found to increase monotonically with all pertinent parameters, while the Richardson number contributed to enhanced flow velocity. However, nanoparticle flux was observed to oppose the flow. Additionally, an increase in the Prandtl number was shown to elevate the velocity profile.

Mahdy and Chamkha [11] investigated in heat transfer and fluid flow of a non-Newtonian nanofluid over an unsteady contracting cylinder employing Buongiorno's mode. The result show that the fluid velocity decreases initially due to increase in the unsteadiness parameter, whereas the temperature and concentration increases significantly, the effect of increasing of Casson parameter is found to suppress the velocity field, the temperature and concentration decrease as the Casson parameter increases and the Prandtl number can be used to increase the rate of cooling in conducting flows.

Siavashi et al. [12] conducted a numerical investigation examining the effects of porous rib arrangement on heat transfer and entropy generation in nanofluid flow through an annulus using a two-phase mixture model. Their results demonstrated that both the permeability and height of porous ribs significantly influence the system's thermal performance. The study revealed that vortex zones alter the entropy variation trends and performance numbers, with local optima existing for these parameters. Furthermore, the research highlighted that nanofluids play a more substantial role in

heat transfer enhancement within recirculating zones at higher volume fractions.

Makinde et, al., [13] investigated the thermodynamic analysis of variable viscosity hydromagnetic Couette flow in a rotating system with Hall effects. Their analysis revealed that fluid rotation enhances heat transfer irreversibility effects in the upper moving plate region, while entropy generation predominates in the lower fixed plate region. Anbuchezhian et al. [14] investigated the combined effects of thermophoresis and Brownian motion on boundary layer flow of nanofluids in thermally stratified systems under solar energy conditions. Their research identified nanoparticle volume fraction as a crucial parameter influencing both flow fields and temperature distributions. The study revealed two key findings which are fluid temperature increases while nanoparticle volume fraction decreases with enhanced Brownian motion, and fluid temperature decreases as thermal boundary layer thickness increases.

This research has significant practical applications, particularly in microelectronics cooling, where it enables precise flow and temperature control with minimal energy loss. Additionally, it can optimize performance in industrial heat exchangers, especially those with permeable surfaces, by improving energy dissipation efficiency. The findings also benefit solar thermal collectors by enhancing natural convection in collector channels, among other potential uses.

The study is novel because it integrates wall permeability effects, entropy generation analysis, buoyancy-driven unsteady nanofluid flow, and convective cooling boundary conditions into a unified model. This approach reveals intricate interactions between these factors and provides new design insights for high-efficiency thermal-fluid systems. Unlike prior studies, which primarily examine steady-state laminar or turbulent forced convection (focusing on first-law energy efficiency), this work investigates unsteady buoyancy-driven flow, introducing temporal complexity. It also treats wall permeability as a design variable influencing velocity and thermal fields while incorporating second-law analysis to assess how permeability affects thermodynamic irreversibility. To streamline the analysis, the study adopts the following simplifications:

- Nanoparticle shape effects are neglected.
- Surface roughness of channel walls is ignored.
- No-slip velocity condition is imposed at the wall, despite permeability.

2 Mathematical Model

This study investigates the unsteady laminar flow of viscous, incompressible nanofluids containing copper (Cu) and alumina (Al_2O_3) nanoparticles through a vertical permeable channel. The system considers heat exchange between the channel walls and surrounding environment following Newton's law of cooling. A Cartesian coordinate system (x, y) is adopted, where x represents the axial direction along the channel centerline and y denotes the normal distance from the centerline, as illustrated in Figure 2. The analysis focuses on the hydrodynamic and thermal behavior of the nanofluid flow under these specified conditions.

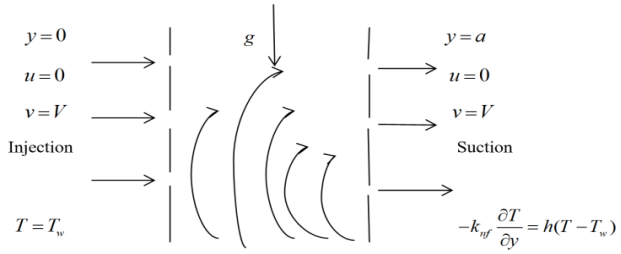

Fig. 2: Schematic diagram of the problem under consideration

The governing equations for one-dimensional transient nanofluid flow in the channel consist of the modified Navier-Stokes momentum equation and energy balance equation, incorporating the Boussinesq approximation. These equations account for the combined effects of viscous forces, thermal buoyancy, and nanoparticle transport phenomena characteristic of the Cu/Al_2O_3 nanofluid system under investigation.

$$\frac{\partial u}{\partial t}+V\frac{\partial u}{\partial y}=-\frac{1}{\rho_{nf}}\frac{\partial P}{\partial x}+\frac{\mu_{nf}}{\rho_{nf}}\frac{\partial^2 u}{\partial y^2}+\frac{g\beta_{nf}}{\rho_{nf}}(T-T_w) \tag{1}$$

$$\frac{\partial T}{\partial t}+V\frac{\partial T}{\partial y}=\alpha_{nf}\frac{\partial^2 T}{\partial y^2}+\frac{\alpha_{nf}\mu_{nf}}{k_{nf}}\left(\frac{\partial u}{\partial y}\right)^2 \tag{2}$$

where u is the nanofluid velocity in the x-direction, T is the temperature of the nanofluid, P is the nanofluid pressure, t is the time, a is the channel half width, T_w is the ambient temperature, μ_{nf} is the dynamic viscosity of the nanofluid, k_{nf} is the nanofluid thermal conductivity, ρ_{nf} is the density of the nanofluid, β_{nf} is volumetric expansion coefficient of the nanofluids and α_{nf} is the thermal diffusivity of the nanofluid as given by Mkwizu at el.,[3].

$$\left.\begin{aligned}
\mu_{nf}&=\frac{\mu_f}{(1-\phi)^{2.5}}\\
\rho_{nf}&=(1-\phi)\rho_f+\phi\rho_s\\
\alpha_{nf}&=\frac{k_{nf}}{(\rho c_p)_{nf}}\qquad \tau=\frac{(\rho c_p)_s}{(\rho c_p)_f}\\
\frac{k_{nf}}{k_f}&=\frac{(k_s+2k_f)-2\phi(k_f-k_s)}{(k_s+2k_f)+\phi(k_f-k_s)}\\
(\rho c_p)_{nf}&=(1-\phi)(\rho c_p)_f+\phi(\rho c_p)_s\\
\beta_{nf}&=(1-\phi)\rho_f\beta_f+\phi\rho_s\beta_s
\end{aligned}\right\} \tag{3}$$

The nanoparticles volume fraction $(\phi = 0$ corresponds to a regular fluid) is governed by the respective densities ρ_f and ρ_s (for the base fluid and nanoparticles), volumetric expansion coefficients (β_f and β_s), thermal conductivities (k_f and k_s) and heat capacitances, $\left(\rho c_p\right)_f$ and $\left(\rho c_p\right)_s$ of the constituents. The initial and boundary conditions for the system are defined as follows:

$$\left.\begin{aligned} u(y,0) &= 0 \\ u(0,t) &= 0 \\ T(y,0) &= T_w \\ T(0,t) &= T_w \\ -k_f \frac{\partial T}{\partial y}(a,t) &= h[T(a,t) - T_w \end{aligned}\right\} \quad (4)$$

Where T_w is the ambient temperature which also corresponds to the lower wall temperature. Table 1 summarizes the thermophysical properties of the base fluid (water) and nanoparticles (copper [Cu] and alumina [Al_2O_3]) at the reference temperature. The tabulated data includes key parameters such as density, specific heat capacity, thermal conductivity, and thermal expansion coefficient, which are essential for modeling the nanofluid behavior under the specified conditions.

Table 1: Thermophysical properties of the base fluid (water) and nanoparticles *[Mkwizu et al.,*[3]]

Physical properties	**Fluid phase (water)**	**Copper (*Cu*)**	**Alumina (*Al_2O_3*)**
c_p (J/kg K)	4179	385	765
ρ (kg/m^3)	997.1	8933	3970
k (W/m *K*)	0.613	401	40
β (K^{-1})	$21x10^{-5}$	$1.65x10^{-5}$	0.85x10^{-5}

The governing equations (1) - (4) are non-dimensionalized using the following dimensionless variables and parameters:

$$\left.\begin{aligned} \theta = \frac{T - T_w}{T_w} \quad \bar{t} = \frac{tV}{a} \quad v_f = \frac{\mu_f}{\rho_f} \quad Ec = \frac{{v^2}_f}{c_{pf} T_w a^2} \\ X = \frac{x}{a} \quad W = \frac{ua}{v_f} \quad \bar{P} = \frac{\rho_f a^2 P}{{\mu^2}_f} \quad A = -\frac{\partial \bar{\bar{P}}}{\partial x} \\ Re = \frac{Va}{v_f} \quad \tau = \frac{\left(\rho c_p\right)_s}{\left(\rho c_p\right)_f} \quad \eta = \frac{y}{a} \quad Pr = \frac{\mu_f cp_f}{k_f} \\ Gr = \frac{\beta_f g T_w a^2}{{v^2}_f} \\ n = \frac{\left(1 - \phi + \phi\beta_s\rho_s/\beta_f\rho_f\right)}{\left(1 - \phi + \phi\rho_s/\rho_f\right)} \quad m = \frac{\left(k_s + 2k_f\right) + \phi\left(k_f - k_s\right)}{\left(k_s + 2k_f\right) - 2\phi\left(k_f - k_s\right)} \end{aligned}\right\} \quad (5)$$

The non-dimensionalized governing equations, along with their corresponding initial and boundary conditions, are expressed as follows:

$$\frac{\partial W}{\partial \bar{t}} = \frac{A}{\mathrm{Re}(1-\phi+\phi\rho_s/\rho_f)} + \frac{1}{\mathrm{Re}(1-\phi)^{2.5}(1-\phi+\phi\rho_s/\rho_f)} \frac{\partial^2 W}{\partial \eta^2} - \frac{\partial W}{\partial \eta} + \frac{Gr\theta n}{\mathrm{Re}} \quad (6)$$

$$\frac{\partial \theta}{\partial \bar{t}} = \frac{1}{m\,\mathrm{Pr}\,\mathrm{Re}(1-\phi+\phi\tau)} \frac{\partial^2 \theta}{\partial \eta^2} + \frac{Ec}{\mathrm{Re}(1-\phi)^{2.5}(1-\phi+\phi\tau)} \left(\frac{\partial W}{\partial \eta}\right)^2 - \frac{\partial \theta}{\partial \eta} \quad (7)$$

with initial and boundary conditions;

$$\left.\begin{aligned} \theta(0,\bar{t}) = 0 \quad \theta(\eta,0) = 0 \\ W(\eta,0) = 0 \\ W(0,\bar{t}) = 0 \\ W(1,\bar{t}) = 0 \\ \frac{\partial \theta}{\partial \eta}(1,\bar{t}) = -mBi\theta(1,\bar{t}) \end{aligned}\right\} \quad (8)$$

The nondimensionalized system contains several characteristic parameters: Re (Reynolds number), Bi (Biot number), Gr (Grashof number), Pr (Prandtl number), Ec (Eckert number), and A (pressure gradient parameter). For numerical solution, the spatial derivatives in Equations (6)-(7) are discretized using second-order accurate central finite difference schemes. This formulation reduces the governing equations to a system of nonlinear ordinary differential equations in the initial value form. The resulting coupled equations are solved iteratively using the Runge-Kutta-Fehlberg adaptive step-size integration algorithm, implemented computationally through MATLAB programming.

3 Numerical Procedures

The nonlinear initial boundary value problem (IBVP) described by Equations (6)-(8) was solved numerically using the method of lines (Na, 1979), a semi-discretization finite difference approach. The spatial domain $\eta \in [0,1]$ was discretized into N uniform subintervals with grid spacing $\Delta\eta = 1/N$ generating N+1 nodal points $\eta_i = (i-1)\Delta\eta$, $1 \le i \le N+1$. Spatial derivatives in the governing equations were approximated using second-order central finite difference schemes. Introducing the discrete approximations $w_i(t) \approx W(\eta_i,t)$ and $\theta_i(t) \approx \theta(\eta_i,t)$, the semi-discrete formulation yields the following system of ordinary differential equations:

$$\frac{dW_i}{d\bar{t}} = \frac{A}{\mathrm{Re}(1-\phi+\phi\rho_s/\rho_f)} + \frac{1}{\mathrm{Re}(1-\phi)^{2.5}(1-\phi+\phi\rho_s/\rho_f)} \frac{(W_{i+1} - 2W_i + W_{i-1})}{(\Delta\eta)^2} - \frac{W_{i+1} - W_{i-1}}{2\Delta\eta} + \frac{Gr\theta n}{\mathrm{Re}} \quad (9)$$

$$\frac{d\theta_i}{d\bar{t}} = \frac{1}{m\,\mathrm{Pr}\,\mathrm{Re}(1-\phi+\phi\tau)} \frac{(\theta_{i+1} - 2\theta_i + \theta_{i-1})}{(\Delta\eta)^2} + \frac{Ec}{\mathrm{Re}(1-\phi)^{2.5}(1-\phi+\phi\tau)} \left(\frac{W_{i+1} - W_{i-1}}{2\Delta\eta}\right)^2 - \frac{\theta_{i+1} - \theta_{i-1}}{2\Delta\eta} \quad (10)$$

with initial conditions,

$$W_i(0) = \theta_i(0) = 0 \ , \ 1 \le i \le N+1 \tag{11}$$

The equations corresponding to the first and last grid points are modified to incorporate the boundary conditions as follows

$$W_2 = W_1 \quad \theta_2 = \theta_1 \quad W_{N+1} = 0 \quad W_N(1 - mBi\Delta\eta) \tag{12}$$

Equations (9) and (10) are first order ordinary differential equations with known initial conditions and were easily solved iteratively using Runge-Kutta Fehlberg integration technique implemented on computer using Matlab.

4 Results and Discussion

In the present study,the pure water has been considered as the base fluid and the nanoparticles used are copper (*Cu*) and alumina (Al_2O_3). The Prandtl number of the base fluid (water) is kept constant at 6.2 and the effect of solid volume fraction is investigated in the range of $0 \le \phi \le 0.3$. Numerical solution for the representative velocity field and temperature field has been carried out by assigning some arbitrary chosen specific values to various thermophysical parameters controlling the flow system (figure 3-14). The detailed discussion and graphical representation of the results of above equations are reported in this section.

4.1 Effects of parameter variation on Velocity profiles

This section analyzes the computed velocity profiles for both Cu-water and Al_2O_3-water nanofluids, examining their response to varying physical parameters. Figures 3 and 4 collectively demonstrate the spatiotemporal evolution of the velocity fields, showing distinct dynamic characteristics between the two nanofluid suspensions as they develop across the domain ($0 \le \eta \le 1$) and progress through dimensionless time. The visualized profiles reveal three key phenomena: (i) differential acceleration patterns between metallic (Cu) and ceramic (Al_2O_3) nanoparticle suspensions, (ii) characteristic boundary layer development modulated by the combined effects of Grashof and Reynolds numbers, and (iii) time-dependent stabilization features that emerge after sufficient elapsed time. Particularly noteworthy is the enhanced momentum transport observed in Cu-nanofluids compared to their Al_2O_3 counterparts under identical thermal and flow conditions, attributable to the superior thermal diffusivity of copper nanoparticles.

The temporal evolution of nanofluid velocities in Figure 3 reveals three critical trends. First, the velocity profiles exhibit a monotonic increase with time for fixed parameter values until reaching steady-state conditions at t=0.25. Second, spatial analysis demonstrates an inverse relationship between velocity magnitude and distance from the channel boundary, with velocities attenuating as η increases.

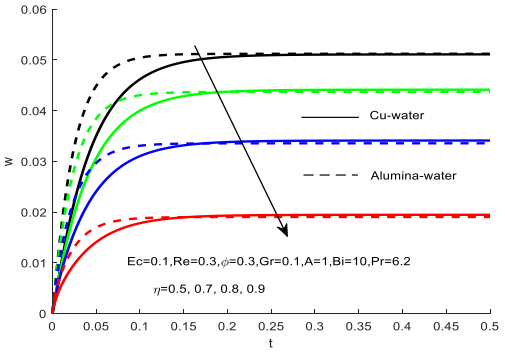

Fig. 3: Nanofluid velocity profile with increasing time (t)

Third, comparative analysis of nanofluids shows that alumina-water (Al_2O_3-H_2O) achieves higher velocities near the left plate (η=0) during the transient phase compared to copper-water (Cu-H_2O). This behavior is attributed to the lower density of alumina nanoparticles relative to copper which reduces inertial resistance in the Al_2O_3-H_2O suspension. The observed steady-state convergence at t=0.25 suggests comparable momentum diffusion timescales for both nanofluids despite their differing transient dynamics.

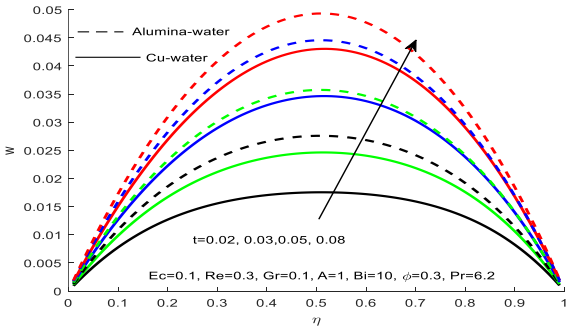

Fig. 4: Nanofluid velocity profile with increasing space (η)

Figure 4 reveals important characteristics of the nanofluid flow behavior within the channel. The velocity profiles show a clear dependence on both time and spatial position, exhibiting progressive acceleration as time evolves while maintaining a distinct parabolic distribution across the channel width. Notably, the maximum velocity occurs along the centerline (η=0.5), with values decreasing symmetrically toward both channel walls (η=0 and η=1), consistent with classical pressure-driven flow behavior. Comparative analysis between the two nanofluids demonstrates that the alumina-water suspension (Al_2O_3-H_2O) achieves consistently higher velocities than the copper-water nanofluid (Cu-H_2O) throughout the temporal development. This performance difference can be attributed to the substantial density contrast between the nanoparticle materials, with copper's higher density resulting in greater flow resistance and consequently reduced velocities compared to the lighter alumina nanoparticles. The observed velocity patterns provide valuable insights into

the momentum transport characteristics of different nanofluid systems in confined channel flows.

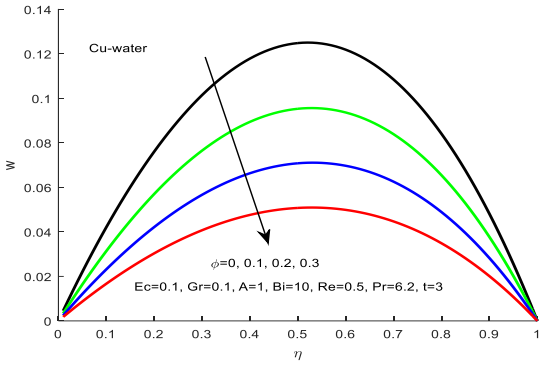

Fig. 5: Nanofluid velocity profile with increasing (ϕ)

Figure 5 demonstrates that increasing the nanoparticle volume fraction (ϕ) leads to a reduction in nanofluid velocity. This behavior can be attributed to two primary factors: the enhanced density and dynamic viscosity of the nanofluid with higher nanoparticle loading, which increases flow resistance, and the influence of fluid suction and injection at the channel walls. Additionally, the velocity profiles exhibit a characteristic parabolic distribution, reaching maximum values at the channel centerline (η=0.5) and diminishing to minimum values at both walls (η=0 and η=1). This spatial variation is consistent with classical pressure-driven flow behavior in confined geometries. The observed velocity suppression at higher ϕ values is particularly significant for engineering applications, as it highlights the trade-off between the potential thermal benefits of nanoparticles and their hydrodynamic impacts. The combination of increased viscosity and density at elevated nanoparticle concentrations, coupled with wall effects, collectively contributes to the deceleration of the nanofluid flow.

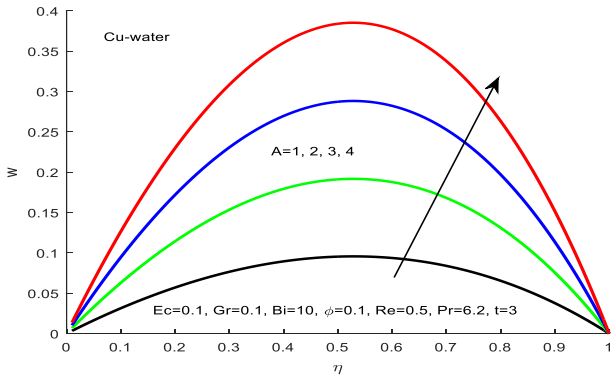

Fig. 6: Nanofluid velocity profiles with increasing (A)

Figure 6 demonstrates the significant influence of the pressure gradient parameter A on nanofluid velocity profiles. The results reveal a direct proportionality between the pressure gradient magnitude and flow velocity, with enhanced momentum transport occurring at higher values of A. The velocity distribution exhibits characteristic parabolic behavior, peaking at the channel centerline (η=0.5) and diminishing to no-slip conditions at both bounding walls (η=0 and 1). This spatial variation manifests that the progressive velocity acceleration along the central flow region with increasing η, reaching maximum values at η=0.5, and the simultaneous velocity attenuation in the near-wall regions due to viscous effects. The observed behavior confirms the expected hydrodynamic response to pressure-driven flow conditions, where increased pressure gradients overcome viscous resistance more effectively, particularly in the core flow region. These findings have important implications for nanofluid system design, suggesting that pressure gradient modulation can serve as an effective control parameter for flow velocity optimization in channel applications.

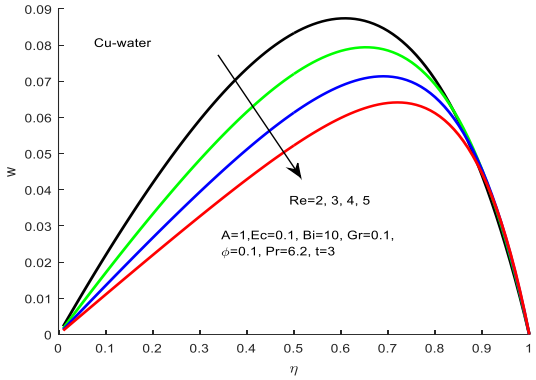

Fig. 7: Nanofluid velocity profiles with increasing (Re)

The velocity profiles in Figures 7 reveal significant Reynolds number (Re) dependence, showing three key hydrodynamic responses. First, increasing Re values consistently reduce the nanofluid velocity magnitude throughout the primary flow region, indicating enhanced viscous dissipation effects at higher flow inertia. Second, this Re sensitivity diminishes markedly near the right channel wall (η → 1), where velocity profiles converge regardless of Re magnitude, suggesting the formation of a viscous-dominated boundary layer that stabilizes the wall-adjacent flow. Third, the characteristic parabolic velocity distribution persists across all Re cases, exhibiting maximum velocities at the channel centerline (η = 0.5) that increase with η until the midpoint, while decreasing sharply near both walls (η = 0 and 1) due to no slip conditions. This spatial behavior reflects the fundamental balance between inertial forces that drive central flow acceleration and viscous effects that dominate near boundaries. The observed Re-velocity relationship has practical implications for nanofluid system operation, demonstrating that while Reynolds number significantly influences core flow dynamics, its control authority becomes negligible in the immediate wall region where viscous forces govern the flow physics. These findings provide valuable insights for optimizing nanofluid applications where both flow velocity and wall shear stress require careful consideration.

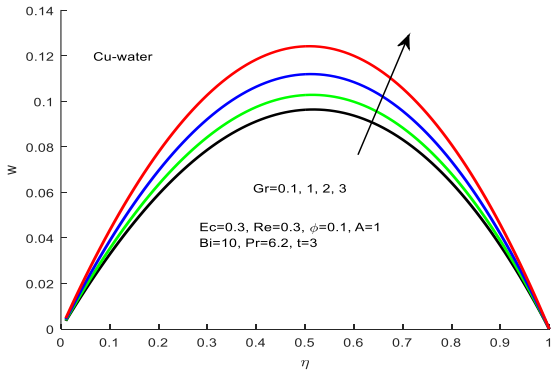

Fig. 8: Nanofluid velocity profiles with increasing (Gr)

Figure 8 demonstrates the significant influence of Grashof number (Gr) on nanofluid velocity profiles, revealing several important hydrodynamic characteristics. The results clearly show that increasing Gr values lead to enhanced nanofluid velocities, a direct consequence of the strengthened buoyancy forces that promote more vigorous fluid motion. This behavior stems from the fundamental relationship between Grashof number and thermal buoyancy effects, where higher Gr values indicate greater buoyancy-driven convection relative to viscous forces. The velocity profiles exhibit a characteristic spatial distribution, reaching maximum magnitudes at the channel centerline (η = 0.5) while diminishing to minimum values at both walls (η = 0 and 1), consistent with classical mixed convection patterns. The observed acceleration at the channel center corresponds to the region where buoyancy effects dominate, while the near-wall deceleration reflects the persistent influence of viscous forces and no-slip boundary conditions. These findings highlight the crucial role of thermal buoyancy in nanofluid flow dynamics, suggesting that Grashof number serves as an effective control parameter for modulating flow characteristics in thermal applications. The consistent parabolic profile across different Gr values further confirms the stable development of thermal boundary layers and their interaction with the momentum boundary layer in buoyancy-assisted flow configurations.

4.2. Effects of Parameter Variation on Temperature Profiles

This section presents a comprehensive analysis of the temperature profiles for copper-water (Cu-H_2O) and alumina-water (Al_2O_3-H_2O) nanofluids, highlighting their response to spatial and temporal evolution under varying physical parameters. Figures 9 and 10 illustrate the distinct thermal behavior of the two nanofluids, revealing several key trends. First, the temperature profiles exhibit a progressive increase with time, reflecting the cumulative thermal energy absorption as the system evolves. Second, spatial variations demonstrate higher temperatures near the channel walls (η=0 and η=1) compared to the centerline (η=0.5), a result of the imposed thermal boundary conditions and heat exchange with the surroundings.

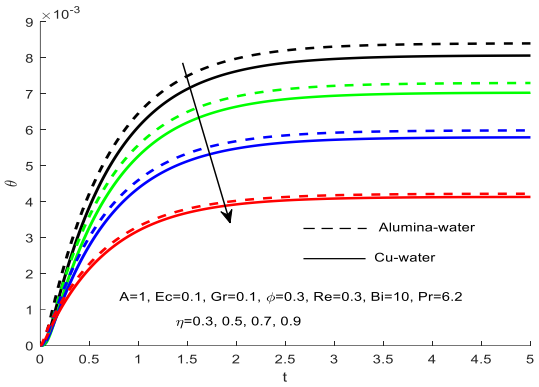

Fig. 9: Nanofluids temperature profile with increasing time (t)

From Figure 9, the temporal evolution reveals that both nanofluids exhibit progressive temperature increases until reaching steady-state conditions at t=3.5. Notably, Al_2O_3-H_2O demonstrates faster thermal response compared to Cu-H_2O, contrary to expectations based solely on thermal conductivity. The spatial distribution shows: the temperature reduction near channel walls (η=0,1) due to Newtonian cooling effects, and the consistent axial temperature decay ($\partial\theta/\partial\eta<0$) for both nanofluids. These observations suggest competing mechanisms where Al_2O_3's lower specific heat capacity may enable faster transient heating despite Cu's superior conductivity.

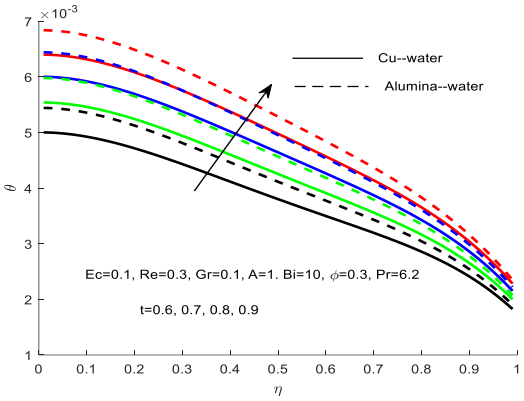

Fig. 10: Nanofluids temperature profile with increasing space (η)

Figure 10 shows that the temperature profiles exhibit dual dependence on temporal and spatial coordinates, showing: the progressive heating with time ($\partial\theta/\partial t > 0$) until thermal equilibrium, and the consistent temperature decay with increasing η particularly pronounced near the right wall (η=1) due to convective losses. Notably, Al_2O_3-H_2O demonstrates faster transient heating rates than Cu-H_2O despite copper's higher thermal conductivity, suggesting dominant influence of nanoparticle heat capacity in time-dependent thermal response. The observed wall-adjacent cooling confirms effective heat exchange with the ambient environment.

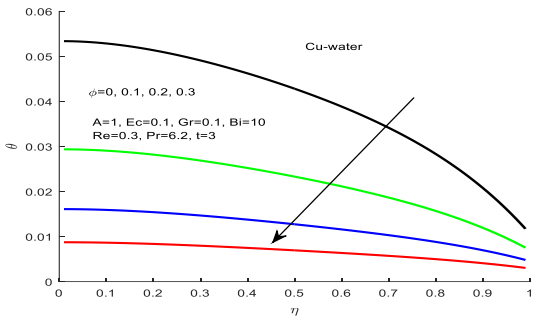

Fig. 11: Nanofluids temperature profile with increasing (ϕ)

Figure 11 display the effects of nanoparticle volume fraction on nanofluid Temperature profile. It is noted that the Temperature of the nanofluid decreases with the increase of nanoparticle volume fraction as other parameters remain constant. Moreover, it is observed that the temperature decreases with the increases of space. Also, it is noticed that there is a decrease in the nanofluid temperature towards the right channel's wall due to convective heat loss to ambient surrounding.

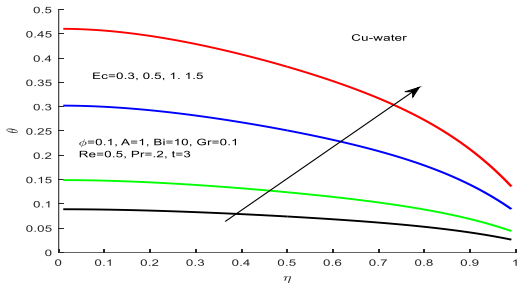

Fig. 12: Nanofluids temperature profile with increasing (Ec)

Figure 12 represent the effect of Eckert number Ec on the nanofluids temperature profile as other parameter remain constant. It is noted that with an increase in Eckert number the nanofluid temperature profile rises. This increase in temperature may be caused by viscous heating effect of nanofluid. Also, it can be noticed that there is a decrease in the nanofluid temperature towards the right channel's wall due to convective heat loss to ambient surrounding. Again, it is observed that the temperature decreases with the increases of space.

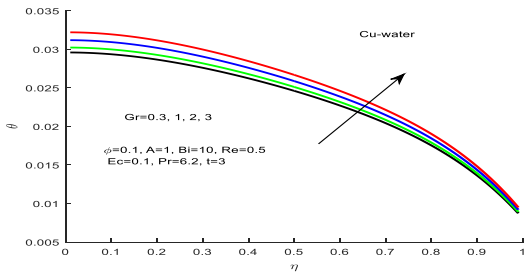

Fig. 13: Nanofluids temperature profile with increasing (Gr)

In figure 13, the effects on the nanofluids temperature profiles caused by Grashof number is displayed. It can be seen from the temperature profile that a rise in the nanofluid temperature is observed with an increase in the value of Grashof number. This happen because increasing Grashofnumber means increasing buoyancy force which enhances the temperature. Also, it can be noticed that there is a decrease in the nanofluid temperature towards the right channel's wall due to convective heat loss to ambient surrounding. Furthermore, it is observed that the temperature decreases with the increases ofspace.

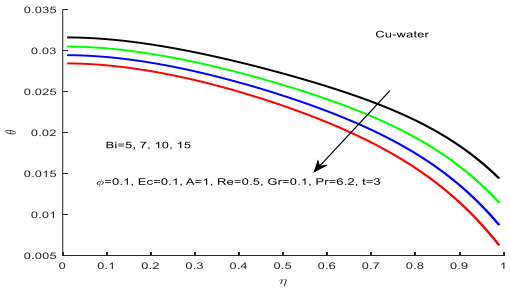

Fig. 14: Nanofluids temperature profile with increasing (Bi)

Figure 14 illustrates the influence of the Biot number (Bi) on the temperature distribution within the nanofluid. The results demonstrate an inverse relationship between Bi and temperature, where increasing Bi values lead to progressively lower temperature profiles. This behavior stems from enhanced convective cooling at higher Biot numbers, which intensifies heat transfer from the channel walls to the surrounding environment. Additionally, the temperature distribution exhibits spatial dependence, decreasing along the channel length. Notably, the right wall region shows more pronounced temperature reduction due to convective heat losses to the ambient. These observations collectively highlight the significant role of Biot number in governing the thermal characteristics of the nanofluid system under convective cooling conditions.

5 Conclusions

This study numerically investigated wall permeability effects on entropy generation in unsteady buoyancy-driven nanofluid flow through a vertical channel with convective cooling. The semi-discretization finite-difference method coupled with Runge-Kutta-Fehlberg integration successfully transformed the governing PDEs into solvable ODEs, revealing critical thermofluidic insights. Al_2O_3-H_2O nanofluid demonstrated superior flow velocities and faster steady-state attainment (t≈0.25) compared to Cu-H_2O, attributed to its lower nanoparticle density. Velocity profiles exhibited characteristic parabolic distributions, maximized at the centerline (η=0.5) and minimized at the walls due to viscous effects, while showing positive dependence on Re, Gr, and pressure gradient (A) but inverse correlation with ϕ. Thermally, Al_2O_3-H_2O's faster

temperature rise despite its lower conductivity highlighted the dominance of heat capacity in transient response. Temperature increased with Ec and Gr but decreased with Bi and ϕ, with notable wall-adjacent cooling ($\eta \rightarrow 1$) from convective losses. These findings provide actionable guidelines for nanofluid system design, suggesting Al_2O_3 for rapid-response applications and Cu for steady-state high-heat-flux scenarios, while emphasizing the need to optimize ϕ and wall permeability for balanced thermal-hydraulic performance.

References

[1] Choi .S. (1995).Enhancing thermal conductivity of fluids with nanoparticles in Developments andApplications of Nonnewtonian Flows;American Society of Mechanical Engineers. New York, USA, pp. 99–106.

[2] Eastman, J. A., Choi, S. U. S., Li, S., Yu, W. & Thompson, L. J. (2001). Anomalously increasedeffective thermal conductivities of ethylene glycol-based nanofluids containing copper nanoparticles. Applied Physics Letters, 78, (6), pp.718–720.

[3] Mkwizu M.H Makinde, O.D & Nkansah-Gyekye, Y (2015b). Second Law Analysis of Buoyancy DrivenUnsteady Channel Flow of Nanofluids with Convective Cooling. Applied and Computational Mathematics. Vol. 4, (3), pp. 100-115.

[4] Gangadhar et al, (2021). EMHD flow of radiative second-grade nanofluid over a riga plate due toconvective heating revised Buongiorno's Nanofluid Model. Arabian Journal for Science and Engineering, Volume 47, pages 8093-8103

[5] Seyyedi et al, (2020). Second law analysis of magneto-natural convection in a nanofluid filled wavy-hexagonal porous enclosure, International Journal of Numerical Methods for Heat & Fluid Flow, Volume 30 Issue 11

[6] Ali A.O &Makinde O.D (2015) Modelling the Effect of Variable Viscosity on UnsteadyCouette Flow of Nanofluids with Convective Cooling. Journal of Applied Fluid Mechanics, Vol. 8, No. 4, pp.793-802.

[7] Mkwizu M.H, Makinde, O.D & Nkansah-Gyekye, Y (2015a). Effects of Navier slip and wall-Permeability on entropy generation in unsteady generalized Couette flow of nanofluids with Convective cooling. U.P.B. Sci. Bull., Series D, Vol. 77, (4), pp. 1454-2358.

[8] Khamis, S, Makinde, O.D & Nkansah-Gyekye, Y (2014). Modelling the Effects of Variable Viscosity in Unsteady Flow of Nanofluids in a Pipe with Permeable Wall and Convective Cooling, Applied and Computational Mathematics. Vol. 3, (3), pp. 75-84.

[9] Bhatti, M.M. Sheikholeslami, M & Zeeshan, A. (2017). Entropy Analysis on Electro-KineticallyModulated Peristaltic Propulsion of Magnetized Nanofluid Flow through a Microchannel. Entropy 19, (9) pp. 481.

[10] Abbas, T., Ayub, M., Bhatti, M.M., Rashidi, M.M & Ali, M.E.-S. (2016). Entropy Generation onNanofluid Flow through a Horizontal Riga Plate. Entropy 18, (6) pp.223.

[11] Mahdy, A &Chamkha, A (2015).Heat transfer and fluid flow of a non-Newtonian nanofluid over an unsteady contracting cylinder employing Buongiorno's model. International Journal of Numerical Methods for Heat & Fluid Flow, Vol. 25 (4) pp. 703 – 723.

[12] Siavashi, M.,Bahrami,H.R.T&Saffari, H (2017). Numerical investigation of porous rib arrangement on Heat transfer and entropy generation of nanofluid flow in an annulus using a two-phase mixture model. Numerical Heat Transfer, Part A ; Applications: An International Journal of Computation and Methodology, Volume 71, (12).

[13] Makinde, O. D. Eegunjobi, A. S. &Tshehla, M. S. (2015). Thermodynamics Analysis of VariableViscosity Hydromagnetic Couette Flow in a Rotating System with Hall Effects. Entropy 17 (11) PP.7811-7826.

[14] Anbuchezhian, N, Srinivasan, K. Chandrasekaran,K& Kandasamy, R (2012) Thermophoresis andBrownian motion effects on boundary layerflow of nanofluid in presence of thermal stratificationdue to solar energy. Appl. Math. Mech. -Engl. Ed., 33(6), 765–780.